

J. ZHANG✉  
Y.T. LI  
Z.M. SHENG  
Z.Y. WEI  
Q.L. DONG  
X. LU

# Generation and propagation of hot electrons in laser-plasmas

Laboratory of Optical Physics, Institute of Physics, Chinese Academy of Sciences, Beijing 100080, China

Received: 20 January 2005

Published online: 4 June 2005 • © Springer-Verlag 2005

**ABSTRACT** Hot electrons are generated in the interaction between intense ultrashort laser pulses with targets. The process depends on the laser intensity, polarization, incident angle, scale length of plasmas and target materials. In this paper, the recent progress on generation and propagation of hot electrons in non-relativistic and relativistic laser-plasma interactions at the Institute of Physics, Chinese Academy of Sciences, are reviewed.

PACS 52.38.Dx; 52.38.Ph; 52.38.Kd; 41.75.Jv; 52.50.Jm

## 1 Introduction

The availability of the high intensity ultrashort laser systems based on the technique of the chirped pulse amplification (CPA) has opened the door to fundamentally new opportunities in science and technology [1]. One of their important applications is in the fast ignition scheme for inertial confinement fusion (ICF), as proposed by Tabak et al. [2]. In Tabak's design, the fast ignition scheme for ICF consists three phases. First, the capsule is imploded to assemble a high-density fuel configuration as in the conventional approach to the inertial fusion. The second phase consists of boring a hole through the corona and pushing the critical density surface close to the compressed core, so that in the third phase, the interacting high-intensity laser pulse can pass the hole without energy loss and hit the high density capsule core to produce abundant energetic electrons triggering the ignition. The latter two phases in the scheme were referred to as the fast ignition concept correspond to two different regimes in the laser-plasma interaction research. The second phase is related to the interaction of intense laser pulses with underdense plasmas, while in the third the ultra-high short laser pulse is interacting with dense plasmas near critical density.

The propagation of the boring laser pulse in the underdense plasma is susceptible to various instabilities, among which, some processes like the stimulated Raman Scattering can produce abundant hot electrons. The hot electrons produced in this phase can preheat or even destroy the compressed core before the arrival of the ignition pulse, and should be avoided. But on other viewpoints, plasma waves related to such in-

stabilities are used to accelerate electrons in the promising new generation of table-top laser-plasma based particle accelerator [3]. The plasma-based particle acceleration has been attracting great interests because plasmas are capable of sustaining extremely large acceleration gradients, which are on the order of the non-relativistic wave breaking limit [4],  $E_0 = cm_e\omega_p/e$ , where  $\omega_p^2 = 4\pi e^2 N_e/m_e$  is the electron plasma frequency with  $N_e$ ,  $m_e$  and  $e$  as the ambient electron density, electron mass and charge, respectively. Taking  $N_e = 10^{18} \text{ cm}^{-3}$  for instance. It gives  $E_0 = 100 \text{ GV/m}$ , approximately three orders of magnitude larger than that obtained principally in the conventional radio frequency linear accelerators (RF linacs). The laser-plasma based accelerator contains two aspects to realize the collimated energetic electron beam. Firstly, a large amplitude plasma wave should be excited. Secondly, the seed electron bunch should be injected into the plasma wave at a proper time so that it can be in phase with the latter. Various schemes have been proposed to excite large amplitude plasma waves by making use of beat waves (PBWA)[3, 5] and laser wake fields (LWFA)[6–9]. The developments of plasma waves and instabilities are usually monitored through measurements of the scattered laser spectrum, on which the  $n$ -th order satellites exhibit at frequencies  $(\omega \pm n \cdot \omega_p)$  with  $\omega$  as the laser frequency [10]. The wave amplitude is limited by the wave-breaking, during which a large number of hot electrons are generated. The process signature is the broadening of the peaks on the scattered laser spectrum. In the scheme of LWFA, when the duration of the driving laser pulse is half of the non-linear plasma wavelength,  $\tau_d = 0.5\lambda_p^{\text{NL}}$ , the laser wake field can be optimally driven to the largest amplitude [11]. The phase velocity of the excited plasma wave can be approximated by the group velocity of the driving laser pulse in the plasma. The de-phasing length, which is defined as the distance relativistic electrons travel when they overrun the driving laser pulse, limits the maximum energy electrons can obtain through non-linear wave acceleration to  $\gamma_{\text{max}} = 4\gamma_p^3 - 3\gamma_p$ , where  $\gamma_p = 1/\sqrt{1 - v_p^2/c^2} \approx \omega/\omega_p$  with plasma wave phase velocity  $v_p$  [12]. Experiments conducted under various conditions have shown that there exist threshold values of plasma density and laser intensity for the plasma wave to reach the stage of breaking. With gas plasmas, by controlling the uniform plasma density and the driving laser pulse intensity just above threshold values, one achieved single mono-energetic electron bunch with energy up to hundreds of MeV and the energy spread less than 3% when only a small

✉ Fax: +86-10-82649356, E-mail: jzhang@aphy.iphy.ac.cn

proportion of electrons break from the wave and the wave structure is maintained but reduced to a smaller amplitude by the electron loading effects [13, 14].

In underdense plasmas, electrons can also be accelerated directly by the intense laser pulse (LDA). People have observed double Maxwellian distribution of hot electrons with the higher effective temperature of 3 MeV and the maximum energy up to 20 MeV [15]. This distribution feature is attributed to intensity enhancement by the relativistic self-focusing of the interacting laser pulse. A betatron resonance acceleration process was predicted by Pukhov et al. [16], and observed in experiments with cluster plasmas [17, 18]. When the plasma density goes further lower and the relativistic interacting laser pulse is sufficiently short so that  $\tau_d \ll \lambda_p^{NL}$ , the interacting laser pulse can rarely experience self-focusing process. This condition also significantly suppress the laser wake field. It is interesting to find that the intense short laser pulse can trap electrons and carry them with it like a soliton-like system. The trapped electron bunch can be extracted by blocking the laser pulse with a plasma separator, as simple as a foil that is thick enough [19, 20].

When the plasma density goes higher to near-critical density as the igniting laser pulse encounters in the third phase of the fast ignition concept, the intense interacting laser pulse is more susceptible to instabilities and most excited waves tend to break, as the growth rate of these instabilities are proportional to the plasma density. Raman Forward Instability, which normally competes with the two plasmon decay instability (TPD) [21] as the laser pulse approaches the region of quarter-critical density. Its growth rate is  $\Gamma_{SRFS} = \frac{\omega_p^2}{\omega} \frac{a}{\sqrt{8(1+a^2/2)}/\sqrt{1-v_{th}^2/c^2}}$ , where  $v_{th}$  represents the electron maximum thermal velocity [?]. We are interested in situations of intense laser beams with sub-ps durations. Using Mori's spatial-temporal theory, the gain of the stimulated instability can be obtained. For a 400 fs, 1.05  $\mu\text{m}$  interacting laser pulse with an intensity of  $10^{19} \text{W/cm}^2$  and a Rayleigh length of 650  $\mu\text{m}$  in plasmas after being focused by an off-axis paraboloid mirror, the gain of SRFS in plasmas with  $\omega_p/\omega = 0.1$  can exceed  $10^3$  and should be able to be observed. Another nonlinear process the interacting laser pulse is likely to experience is self-focusing, which may be due to the relativistic effects when its power exceeds the critical value  $P_c \approx 17(\omega_p/\omega)^2$  [23, 24], or due to the density fluctuation in preformed plasmas. The interacting laser pulse is also very likely to suffer the stimulated Brillouin scattering (SBS) [25]. Scattering or decaying mechanisms of driving pulses play detrimental roles in the fast ignition concept as they scatter a significant portion of laser pulses and reduce the coupling of laser energy into the fuel capsule. Techniques using combined spatial, temporal and polarization beam smoothing were introduced to improve the beam uniformity and effectively reduced SBS and SRS. Based of physical experiments, those processes render the interpretation of experimental results a complicated work. Models have to be invoked for understanding of possible mechanisms underlying the observation. Experiments with strictly controlled conditions need to be conducted for proof of even a simple theoretical prediction.

This review article mostly concentrates on experimental works about intense short laser pulse interaction with plasmas from flat solid targets. Reasons for studies on this interaction regime is partially because this subject is very important to the fast ignition concept of the inertial confinement fusion and because the physical rules obtained under long laser pulse approximation are confronted with suspicious arguments about their applications in the interpretation of phenomena observed in ultra-short high intensity CPA laser experiments.

Experiments were carried out mainly at the Laboratory of Optical Physics of the Institute of Physics, CAS. The laser systems include home-made XL (Extreme Light) series, which can deliver 50–650 mJ energy in a 30 fs FWHM duration. The contrast ratios of laser pulses with different energy are well controlled under  $10^{-5}$ – $10^{-4}$ . Home-built laser pulse diagnostics, such as SPIDER, FROG and single-shot auto-correlator, are used to monitor every laser pulse incident on the target. The focusing geometry mainly consists of an off-axis paraboloid mirror and focus spot monitoring systems. In experiments, we controlled plasma density profiles by introducing pre-pulses in advance of the interacting pulse. Shadowgraphy and interferometry techniques are applied to measure the plasma density profile. The plasma density profile are approximately exponential with scale length varying from ten percent of laser wavelength  $\lambda$  to tens of  $\lambda$ s. Details of the experiments setup are described in Sect. 3.

In experiments, large numbers of energetic electrons are known to be generated. Measurements and characterization of the energetic electron emission is important because it provides useful information about the interacting mechanism (producing mechanism). For a single electron, its behavior and trajectory are determined by the intensity, shape and polarization state of the laser pulse. In a sub-relativistic laser intensity of  $I\lambda^2 < 1.37 \times 10^{18} \text{W/cm}^2$  ( $a \ll 1$ ), where  $I$  is the laser intensity in  $\text{W/cm}^2$ , and  $\lambda$  is the laser wavelength in  $\mu\text{m}$ , the electron mainly responds to the electric component of the laser pulse. The magnetic component plays an increasingly important role as the intensity of the laser increases. When  $a \sim 1$ , electric and magnetic components exert forces of the same order on the electron and push it along the gradient direction of the laser intensity as the electron quivers in the polarization plane [26]. While with plasma targets, behavior of electrons in laser fields is determined by the combination effects of the laser field and collective plasma functions. The production mechanisms of hot electrons are rather difficult to identify. For example, the component of the non-relativistic laser electric field along the plasma density gradient can resonantly drive the plasma wave to break, producing large amount of hot electrons with an effective temperature larger than  $T_H \sim 6 \times 10^{-5}(I\lambda)^{0.33} \text{eV}$  [27] deduced for long pulse approximation. While for a relativistic laser intensity of  $I\lambda^2 > 1.37 \times 10^{18} \text{W/cm}^2$  ( $a > 1$ ), the laser ponderomotive force or  $\mathbf{V} \times \mathbf{B}$  force dominates the interacting mechanism with a solid density plasma. Such interaction produces hot electrons with a Maxwellian distribution characterized by an effective temperature the same as the laser ponderomotive potential  $T_H \sim 0.511 \times (\sqrt{1+a^2/2} - 1) \text{MeV}$  [28]. Electrons are mainly accelerated in the longitudinal direction. If a large scale length pre-plasma is formed before the

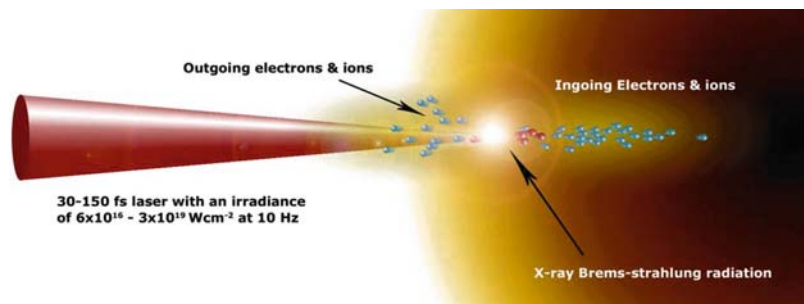


**FIGURE 1** Generation and transport of hot electrons produced in the ultrashort and ultra-intense laser – plasma interactions

main beam arrives, the interacting process can be much more complicated. Various parametric instabilities as well as other mechanisms such as stochastic heating [29] and plasma wake wave may also accelerate electrons, as discussed above for the under-dense plasmas [30]. Each interacting mechanism has its own characteristics manifested by the hot electron emissions.

The generated hot electrons can be roughly divided into two groups, according to their emission directions. One group of them eject backward into the vacuum through the under-dense plasma. Others transport forward into the over-dense plasma region and the cold target remains, where hard x-ray photons are produced through Bremsstrahlung process. When using a foil target, hot electrons can exit from the rear of targets, where a strong space-charge field is setup and accelerates ions to high energy. A schematic picture showing the physics is illustrated in Fig. 1.

This review is organized as follows. In Sect. 2, we describe in detail the home-made XL series since our research works require complete control of the laser pulse characteristics. The experiment setup including the plasma diagnostics is shown in Sect. 3. Section 4 recalls, respectively, the effects of the laser polarization and the plasma density scale length on the hot electron emission in experiments with non-relativistic laser pulses. Studies of the propagation of hot electrons in plasma and solid targets is also presented. In Sect. 5, the relativistic laser intensity and pulse duration effects on hot electrons are discussed. Experiments with unique plasma density profiles produced from targets of specific features such as micro-water droplets are dealt with in Sect. 6. These kinds of experiments with neutron generation are demonstrated as a promising ‘table-top’ neutron source. Sect. 7 summarizes this whole review, and the prospects of Hot Electron subject are discussed.

## 2 The multi-terawatts femtosecond Ti:sapphire laser system

As the experimental platform for high field physics research, a 20TW CPA Ti:sapphire laser system (XL-II), with recently improved techniques was designed and constructed, delivering an energy up to 640 mJ within a pulse duration of about 31 fs. As successor of the home-made 1.4TW Ti:sapphire lasersystem XL-I [31], in the newly built XL-II laser system, an adaptive optics system is used to correct the wave-front of the compressed laser pulses. The optimized beam quality makes it possible to realize 1.5 times diffraction limits when focused by an off-axis parabola, providing a focused power density of  $10^{19}$  W/cm<sup>2</sup>. In this section, we describe the design and the performance on the 20TW Ti:

sapphire laser. The seeding pulse is released by a Kerr-Lens Mode-locking (KLM) Ti:sapphire laser (the oscillator). After the Martinez telescope stretcher, the 300 ps chirped pulse is amplified up to 640 mJ by a regenerative amplifier and a multi-pass amplifier. The compressor in the vacuum then compresses the pulse into 31 fs.

### 2.1 Oscillator

The Kerr-Lens Mode-locking (KLM) Ti:sapphire laser applies a gain medium of a high-doped Ti:sapphire crystal of 4 mm length (Shanghai Institute of Optics and Fine Mechanics, SIOFM). Different from the scheme in XL-I, we fold the longer arm by two mirrors and the shorter arm by one mirror. A pair of Brewster angle cut fused silica prism is used to control the dispersion of the gain medium in the long arm, between which the effective light path from tip to tip is about 54 cm. This design makes the oscillator very compact and stable. Pumped by a 4.2 W 532 nm laser (Millennia, Spectra-Physics Inc.), mode-locking pulses of shorter than 18 fs can be achieved with an average power of 500mW after careful alignment. The fluctuation of the mode-locking power is less than 1%. Figure 2a and b show the autocorrelation trace and the spectrum of laser pulses.

### 2.2 Stretcher

The applied Martinez stretcher consists of a holographic diffraction grating (Spectrogon AB Inc., Sweden) with a groove frequency of 1200/mm, a concave mirror with the curvature radius of 1 meter and a plane plate. Both the concave mirror and the plane plate are coated with gold, and separated with each other by 0.5 m. To obtain a large stretching of the seeding pulse, we simulated the dispersion with ray tracing method. We calculated the characteristics of the dispersion versus the incident angle and the distance from the grating to the concave mirror. With the optimized parameters, the pulse duration can be stretched to about 300 ps.

### 2.3 Amplifiers

In general, the energy of the seeding pulse is only several nano-joules after the stretcher. To boost the chirped pulse for the application of high field physics, normally a pre-amplifier is first used to supply a large gain for the seeding pulse. The pre-amplifier may be a multi-pass or a regenerative configuration; both can amplify the pulse with a gain of around  $10^6$ . With the multi-pass as the pre-amplifier, the seeding pulse

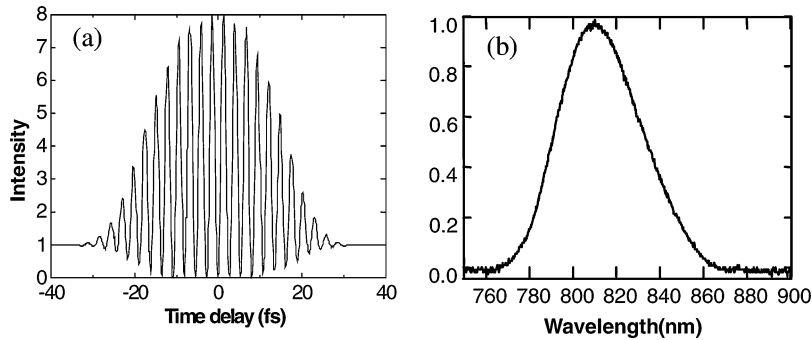


FIGURE 2 Autocorrelation trace **a** and spectrum **b** of the laser pulse from oscillator

can experience low material dispersion and avoid gain-narrowing effect. However, the alignment will be more difficult if an efficient pump is pursued [31]. The output beam quality is also worse. For this reason, we used a typical regenerative resonator as the pre-amplifier in the EX-II laser system. In practice, the seeding pulse is rotated to S-polarization and then coupled into the resonance cavity by the surface reflection of the Ti:sapphire rod. By controlling the synchronous electronics, the voltage on the Pockels cell, and the time delay between the injection and the extraction of the seeding pulse, the 29 trips amplification of the seeding pulse inside the regenerative cavity is realized. The amplified pulse is then dumped out by the thin film polarizer (TFP). With 25 mJ pumping energy (Spectra-Physics, LAB-130-10), the optimized output energy around 4 mJ is achieved. We monitored the amplification process by analyzing with a photodiode and an oscilloscope the leaking light behind the back mirror.

To further boost the pulse energy to Joule level, two or three multi-pass stages are usually used in the conventional designs [32]. Considering that the multi-stage amplification can result in more material dispersion and higher cost of construction, we used only one stage multi-pass main amplifier in XL-II. The Frantz–Nodvick simulation shows that the optimized conversion efficiency occurs around the pumping energy flux of 1 J/cm<sup>2</sup> [33], whilst a higher flux can lead to the gain saturation as well as the optical damages. Based on the above conclusion, we exert much effect on realizing a better mode match between the pumping and the being-amplified lasers, which also support the efficient conversion with one stage main-amplifier. We enlarge the laser beam to a diameter of 14 mm with a Galilean telescope before the multi-pass amplification. A Pockels cell is inserted in the laser path to eliminate the ASE and rotate the S-polarization to the P-polarization. Pumped with two 1.4 J Nd:YAG lasers at 532 nm (Spectra-Physics Inc., Pro-350-10), we obtained an amplified output energy more than 1 J after six passes. It is very critical for the optimized output energy to have a careful control of the synchronous timing and the accurate alignment for the overlap of the seeding pulse and the pumping pulses.

The relay imaging pipes can improve the quality of the beam pattern and increase the energy of the amplified laser pulses. The output laser beam characteristics with and without relay imaging are compared. Without the pipes, the amplified energy is only about 700 mJ. The beam pattern is un-uniform and the last mirror in the six-pass amplifier is easy to be damaged.

## 2.4 Compressor

We build the compressor with a standard configuration based on Treacy's design and put it inside a vacuum chamber. Since the damage threshold of the holographic grating is only about 300 mJ/cm<sup>2</sup>, we once again enlarge the beam diameter to 30 mm before the input window of vacuum chamber. With the total dispersion of the stretcher and transparent optical components, we calculate the optimized parameters for the compressor by combining the ray tracing method and Treacy's equations [34]. Our numerical simulation of the pulse profiles with different incident angles and distances between two gratings indicates that the compressed pulses with a shorter duration and a higher contrast ratio in the leading can be realized by using the mismatch grating pair with the different groove from the stretcher.

This pair of gratings used in the compressor has grooves of 1500 lines/mm (Spert AB). By optimizing the distance between two gratings and the incident angle, we can achieve 31 femtosecond laser pulses with energy up to 640 mJ. Figure 3 is the typical autocorrelation trace (a) and the corresponding spectrum (b) of the output laser pulse. The time bandwidth is about 315 with Sech square assumption. The typical energy stability is less than 3%. Compared to the conventional CPA techniques, the new design using this two-stage amplifier well demonstrates a 20 TW Ti:sapphire laser system with a simplified configuration and a compact size, which supports shorter pulse duration, higher stability, better beam pattern and lower cost.

## 2.5 Adaptive optics system

Many efforts for the higher intensity are concentrated on increasing output energy, reducing pulse duration and temporally cleaning the pulses in the CPA systems. However, in many experiments, the wave-front distortions are also crucial elements to stop reaching higher intensities. In XL-II, we apply an Adaptive Optics System (AOS) to correct the wave-front distortion after the compressor. The AOS consists of a Shack–Hartmann wave-front sensor, a deformable bimorph mirror and a set of electrical control unit. One beam splitter is used to get a small portion from the interacting laser pulse into the Shack–Hartmann wave-front sensor. The control unit obtains the data from the sensor, compares them with an ideal wave-front, and then supplies a correcting signal to drive the deformable mirror. This process repeats itself till

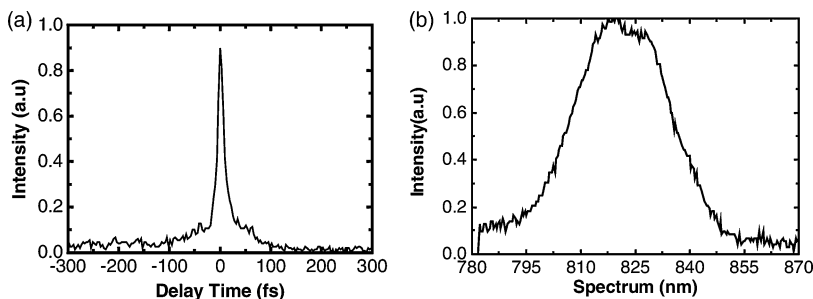


FIGURE 3 Autocorrelation trace **a** and spectrum **b** of the final laser pulse after compression

an ideal wave-front is obtained for the experiments. To avoid the possible nonlinear effect in the air, the deformable mirror and the beam splitter are put in a vacuum chamber, which is connected to the target chamber where physical experiments are conducted.

Setting the energy at 60 mJ and using a 4 m focus lens, the focusing spot is about 432  $\mu\text{m}$  in an average diameter before running the adaptive optics system. It corresponds to about 3.5 diffraction limits. After running the adaptive optics system, the focusing spot is about 200  $\mu\text{m}$  and corresponds to 1.5 times diffraction limits. The beam pattern of the focus spots was recoded by CCD camera. By running the AOS, the beam quality improvement is significant.

### 3 Diagnostics for physics experiments

The whole experimental setup is illustrated in Fig. 4. Laser pulses of 31 fs can be split into successive two parts separated by a variable time period, acting as pre-pulse and interacting pulse, respectively. Circularly and linearly (*s*- and *p*-) polarized incident laser pulse can be obtained by using wave plates. With an off-axis paraboloid mirror of  $f/\# = 3$ , more than 75% of the laser pulse 650 mJ energy can be collected into the focal spot with a diameter less than 15  $\mu\text{m}$ , providing an intensity near  $10^{19} \text{W}/\text{cm}^2$ . We monitored the focus spot with a pin-hole camera. A typical hard x-ray image is shown in Fig. 4 as inset. Usually, we used flat solid targets in experiments. The laser-plasma interaction with clusters,

micro- liquid droplets and foam targets were also studied. Instruments were built to produce clusters of various sizes. The same device can also provide us with water or ethanol micro-droplets.

The main diagnostics include one  $\gamma$ -ray spectrometer to measure radiation up to a few hundred keV. The spectrometer consists of a NaI detector, a photo-multiplier, an amplifier and a multi-channel energy analyzer. In order to eliminate the noise caused by the random  $\gamma$ -ray scattering and enhance the ratio of signal to noise, this assembly was fully enclosed by a Pb cylinder with a 10-mm-diameter hole in the 50-mm-thick cross surface close to the rear of the target, between which an electronic pulsed gate in front of the detector was installed and synchronized with the main laser pulse, as shown in Fig. 4. The NaI detector of the spectrometer is placed 360 mm away the target, indicating a collecting solid angle around  $4 \times 10^{-4}$  sr from the source. The spectrometer had been calibrated using a  $\gamma$ -ray source  $^{22}\text{Na}$  ( $\sim 511$  and  $1270$  keV) [35]. A second shielded NaI detector was used to monitor the stability of  $\gamma$ -ray photon yield for each shot, providing a cross calibration with the first one. A 4-mm-thick aluminum filter was used before the second NaI detector to remove  $\gamma$ -rays below 30 keV. To avoid overlap of photons in detectors, the distances between the detectors and the plasma and the diameter of the hole in the lead block in front of the detectors were adjusted so that the probability of detecting a  $\gamma$ -ray photon for each shot is less than 0.2. The detector response was also checked with calibrating  $\gamma$ -ray sources.

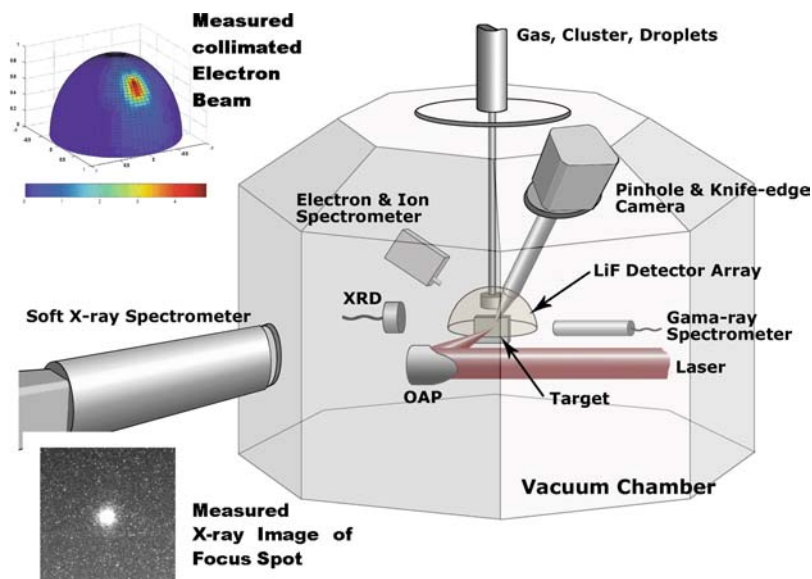
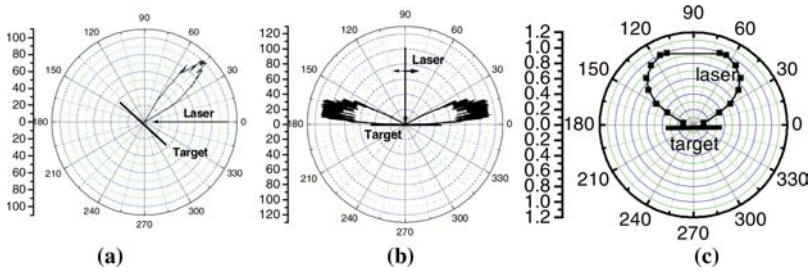


FIGURE 4 Experimental setup. The focus spot x-ray image is also shown as inset, as well as the measured well-collimated hot electron beam with energies greater than 250 keV from ultrashort laser interaction with plasma at an intensity of  $1 \times 10^{16} \text{W}/\text{cm}^2$



**FIGURE 5** The angular distribution of outgoing fast electrons with energies over 50 keV in the incident plane for  $p$ -polarized laser **a**, in the plane perpendicular to the incident plane for  $s$ -polarized laser **b** when laser intensity is  $2 \times 10^{16} \text{ W/cm}^2$ . Also for  $s$ -polarization, when the laser intensity is increased to be  $4 \times 10^{17} \text{ W/cm}^2$  the two peaks shift to the opposite direction of the incident laser beam **c**

A magnetic spectrometer was used to measure the fast electron energy distributions [36]. It is mainly configured with a permanent uniform magnetic field of  $B \sim 380 \text{ G}$ . An array of LiF thermo-luminescent dosimeter (TLDs) detectors at the rear can record hot electrons [37]. The energy range of this instrument covers from 7 to 500 keV, with a resolution better than 2%. The collection angle of the spectrometer was on the order of  $1 \times 10^{-3} \text{ sr}$ . Because the TLDs are insensitive to visible lights, it is not necessary to use aluminum foils in front of the TLDs. The background signal of TLDs is less than  $1.2 \mu\text{Gy}$  after annealed by heating to  $240^\circ\text{C}$ .

Hot electron angular distributions are measured by spherically installed hundreds of TLDs or radiochromic film pieces around the target. The distance from the focus to the TLDs detectors was 45 mm. The angular resolution of the system was about  $6^\circ$ . The expected electron energy range was chosen by composite filter in front of detectors. The filter assembly consisted of aluminum films with different thickness. For some shots, pieces of 1 mm thick CR39 was added at the top as an ion detector. A strong magnetic field was applied in the direction of strong emission signals in order to determine the effects of the x-ray as necessary. One example of the measurements is presented in Fig. 4 as inset, showing one collimated electron beam with the divergence less than  $15^\circ$  [38].

We determined the absorption of the laser pulse by recording the scattered and specularly reflected laser light with  $4\pi$  arranged calorimeters, before which a 2-mm thick quartz plate is installed to block charged particles and x-rays. In some experiments, the low-order harmonics of the laser were analyzed with a monochromatic meter. Crystal spectrometers are used to record the plasma self-emission of x-rays, from which the ionization states of the target materials are obtained.

#### 4 Hot electrons from non-relativistic ultra-short laser interaction with solid targets

In this section, we will discuss the effects of laser polarization and pre-plasmas on generation of hot electrons by ultra-short laser pulses interaction with solid targets. The propagation of the hot electron in the solid target are studied experimentally.

##### 4.1 Polarization effects on the backward hot electrons with laser-solid targets

With moderately intense laser pulses ( $\sim 10^{16} \text{ Wcm}^{-2}$ ), the electric force dominates the interaction mechanisms. Experiments devoted to the studies of the

polarization effects used solid targets, allowing us to produce plasmas with steep or exponential density profiles.

Figure 5a shows the angular distribution of fast electrons generated from an exponentially profiled plasma by  $p$ -polarized laser light in the incident plane at a laser intensity of  $2 \times 10^{16} \text{ W/cm}^2$  [39]. Almost all of the outgoing fast electrons were emitted in the normal direction. The emission direction of the fast electrons obeys the momentum conservation [40]. However, when the solid target was irradiated by a  $s$ -polarized laser pulse, the behavior of the fast electrons differed greatly from the behavior of that generated by  $p$ -polarized laser pulses. As Fig. 5b shows, the outgoing fast electrons were found to be collimated along the laser polarization direction in a plane perpendicular to the incident plane. In the incident plane, no fast electrons were measured. It was also found that the fast electrons with higher energies have narrower angular divergence. When there was a corona pre-plasma in front of the target, a very small percentage of outgoing fast electrons could be found in the incident plane. This suggests that the outgoing fast electrons were mainly accelerated by the electric field of the  $s$ -polarized laser pulses. When there is a corona preplasma in front of the overdense plasma, the possible modulation of the critical surface of the preplasma will steer a very small percentage of the fast electrons out of the polarization direction. This phenomenon seems to be similar to the results of laser accelerator injector based on laser ionization and the ponderomotive acceleration of electrons in gas, where electrons are accelerated in the polarization direction [41, 42], but the heating mechanisms are obviously different. More interestingly, when the laser intensity is increased to  $\sim 10^{17} \text{ W/cm}^2$ , the two peaks shift to the opposite direction of the incident laser beam [43]. An example of  $4 \times 10^{17} \text{ W/cm}^2$  is shown in Fig. 5c. This indicates that the ponderomotive force begins to play a role in producing the electron jets [44].

##### 4.2 Effects of plasma density scale on hot electrons with laser-solid targets

It is well known that when a long laser pulse of nano/picosecond duration interacts with a plasma, the plasma density profile will evolve with time. The evolution includes corona plasma expansion and ponderomotive steepening near the critical surface [45]. However, when an *ultrashort* laser pulse interacts with a plasma, the very short duration does not allow significant evolution of the plasma. There has been a great deal of recent interest in laser absorption and x-ray emission from solid targets irradiated by ultrashort laser pulses [46–48], where the plasma density scale length can

be much less than the laser wavelength  $\lambda_0$ . Similarly, if such an ultrashort laser pulse interacts with a solid target with a preformed plasma in front of it, the interaction will depend, to a large extent, on the properties of the preformed plasma, particularly its scale length. By using a carefully controlled prepulse, one can create any desired plasma density scale length by controlling the time interval between the prepulse and the main pulse. Therefore, an ultrashort laser pulse allows for “clean” interaction with a preformed plasma without significant dynamic evolution of the latter, providing a unique opportunity for identifying the various interaction processes that depend strongly on the plasma density scale length [49–54]. For example, it has been demonstrated that high harmonic generation [49] and angular dependence of the fast-electron and x-ray emission [50] from solid targets depend strongly upon the scale-length.

Here, we investigate the effects of the plasma density scale length on laser absorption, x-ray emission, and hot electron by varying the time gap between the main pulse and the prepulse over a very wide range, from 0 to 275 ps. This corresponds to varying the density scale length from 0 to 11  $\mu\text{m}$ . Mainly in experiments,  $45^\circ$  p-polarized short moderately intense laser pulses were used, while results from s-polarized situations are also invoked for aim of comparisons. We demonstrate the existence of clearly defined multiple absorption peaks and the corresponding peaks in x-ray production and hot electron temperature. The multiple absorption peaks are identified as originating from the transition of the principal absorption mechanisms as the density scale length is increased, namely from vacuum heating/resonance absorption to parametric instabilities. As expected, over the same range only one absorption peak is observed at relatively large scale-length for s-polarized irradiation.

In the experiments, a carefully controlled prepulse with variable time separation from the main laser pulse was used to create preplasmas with different density profiles. Figure 6 shows the measured absorption of laser energy as a function of the scale length  $L$  of the plasma. For p-polarized irradiation, three local peaks of absorption, at about  $0.2\lambda_0$ ,  $2.8\lambda_0$ , and  $5.5\lambda_0$ , were found. Note that there is considerable absorption even without a prepulse. This agrees with the experimental results for aluminum targets at comparable laser intensity [47]. It is apparent that due to vacuum heating [55] and collisional absorption [46], there is absorption even at very small  $L$  (corresponding to a step-like density profile). The absorption decreases significantly when the main pulse immediately follows the prepulse. With increase of  $L$ , an absorption peak at  $0.2\lambda_0$  appears. This can be attributed to resonance absorption at  $L = 0.2\lambda_0$  [45, 51]. When increasing the scale length to more than  $2\lambda_0$ , other peaks appear. To our knowledge, this is the first time that additional peaks of absorption at large scale lengths were observed. Corresponding to the absorption peaks, there are also three main peaks in the Bremsstrahlung x-ray emission (Fig. 7). On the other hand, for s-polarized incidence there is only one absorption peak at  $L = 5.8\lambda_0$ , and only one main peak (at relatively large  $L$ ) in the Bremsstrahlung x-ray emission.

Angular distribution measurements showed collimated jet emission of hot electrons at different scale lengths. We found that the direction of hot electron emission changed dramati-

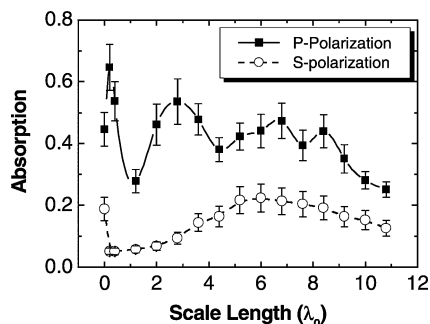


FIGURE 6 The absorption of laser energy as a function of scale length  $L$  (in  $\lambda_0$ ) for p-polarized irradiation (solid square) and s-polarized irradiation (shallow circle) with an incident angle of  $45^\circ$

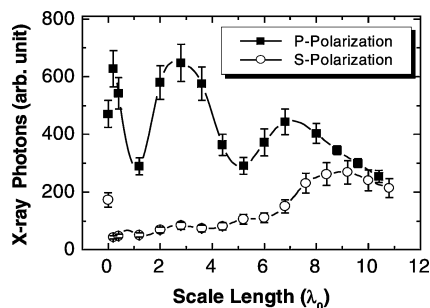


FIGURE 7 The X-ray emission counts as a function of scale length  $L$  (in  $\lambda_0$ ) for both p (solid square) and s-polarized (shallow circle) irradiation with an incident angle of  $45^\circ$

cally as  $L$  is increased from zero. Interaction between an ultrashort laser pulse and a plasma of steep density profile ( $L = 0$ ) produced a very collimated jet at the specular reflection direction, similar to that observed in Fig. 5. As  $L$  is increased, emission in the specular direction decreased abruptly and a sharp collimated jet of hot electrons appeared in the normal direction [39]. The angular divergence of the hot electrons also decreased with increasing hot electron energy. As the absorption reached the local peaks at  $L = 0.2\lambda_0$ ,  $2.8\lambda_0$ , and  $5.5\lambda_0$ , we observed the corresponding local minima in the angular divergence of hot electron emission for p-polarized irradiation.

The increased absorption and x-ray production for the larger ( $L > 2\lambda_0$ ) scale lengths imply the presence of different absorption mechanisms that predominate in the preformed plasma with large density scale lengths. Among the possible mechanisms, linear vacuum heating and nonlinear  $\mathbf{J} \times \mathbf{B}$  type mechanisms can be ruled out since they usually appear only for plasmas with a scale length less than one laser wavelength [55]. On the other hand, Stimulated Raman Scattering (SRS) and two-plasmon decay (TPD) instabilities, together with inverse Bremsstrahlung absorption, can dominate for both p and s-polarized irradiation. Indeed, the correlation between the hot electron generation/Bremsstrahlung x-ray emission and TPD/SRS was evident in our experiments, where clear TPD/SRS spectroscopic signatures at  $3\omega_0/2$  and  $\omega_0/2$  were observed for larger scale lengths in the specular and backward directions.

To confirm the experimental observations and identify the mechanisms for increased absorption in the preformed plasma at long scale lengths, we have carried out a series of numerical PIC simulations for oblique incidence of the laser pulse. In

the simulations, we used targets composed of a high-density region at  $6n_c$  and a preformed plasma which decreases exponentially from the high density platform with variable scale length  $L$ . The temporal profile of the laser pulse has a sine-squared shape with a duration of 50 laser cycles and a Gaussian cross section with a beam diameter of  $10\lambda_0$ . The resulting absorption as a function of  $L$  is given in Fig. 8 for a normalized laser field amplitude of  $a_0 = 0.2$  and  $0.6$ . Several absorption peaks were observed for  $p$ -polarized radiation. The first one is at  $L \sim 0.2\lambda_0$ , consistent with experimental observations, can be attributed to resonance absorption as it is at the optimum scale-length for optical resonance for 45 degree incidence angle. The second one is at  $L \sim 3\lambda_0$ , also in good agreement with the experimental results shown in Figs. 6 and 7. Other absorption peaks can be seen at larger scale lengths, also in agreement with the experiments. The latter peaks may be attributed to stimulated Raman scattering (SRS) and two plasmon decay (TPD) instabilities excited near the quarter critical density. Both instabilities can increase absorption and generate hot electrons for  $L > \lambda_0$ . To confirm this, we monitor the frequency spectra of the reflected light and the backscattered light of the incident pulse. As the scale length increases, the high harmonic emission decreases, as shown in Fig. 9a–d. Meanwhile, emission near  $\omega_0/2$  both around the backward and specular directions, as well as that near  $3\omega_0/2$  around the specular direction appears. TPD occurs first since it has a lower threshold than SRS for the same density gradient [45]. The density perturbation shown in Fig. 9e for  $L = \lambda_0$  is associated with TPD as it is at the quarter critical density and its wave vector is along the  $y$ -direction, agreeing with the theory [56] for oblique incidence. At large scale lengths, such as  $L = 6\lambda_0$ , emission at  $3\omega_0/2$  becomes weak, and emission at  $\omega_0/2$  becomes blue-shifted as compared to short scale-length case. This is an evidence of strong SRS below the quarter critical density, as is further confirmed by the density perturbation appearing in Fig. 9f. Normally one can expect both instabilities to appear [56]. For  $s$ -polarized irradiation, there is almost no collisionless absorption at short scale lengths. However, considerable absorption is found for  $L > 3\lambda_0$ , as shown in Fig. 8. There is only one absorption peak, which can be attributed to mechanisms similar to that for the  $p$ -polarized light at large scale lengths. Non-monotonic absorption curves have also been observed in PIC simulations for normal incidence of laser light [53]. We note that the absorption rates found from PIC simulations are usually lower than that in the experiments. This could be partly attributed to the lack of a suitable description for collisional absorption in the code [47].

Figure 8 also shows the absorption as a function of  $L$  for a normalized laser field amplitude of  $a_0 = 0.6$ . One can see the multippeak structure exists only for the lower laser intensities.

In summary, we have studied the absorption of ultrashort laser pulses in plasmas for a wide range of density scale lengths produced by carefully controlling the time gap between the prepulse and the main pulse. Our experimental results show the important effects of the plasma scale length on the laser-plasma interaction process. Three distinct absorption peaks appear as the density scale length is increased. The enhanced absorption, x-ray emission, and hot electron temperature at large scale lengths for both  $p$ - and  $s$ -polarized lasers are confirmed to be due to parametric instabilities.

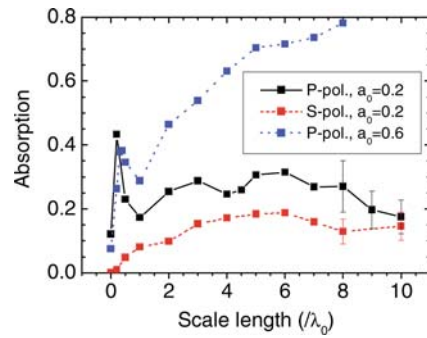


**FIGURE 8** Absorption as a function of the scale length  $L$  (in  $\lambda_0$ ) obtained by 2D PIC simulations for  $a_0 = 0.2$  and  $0.6$

### 4.3 Studies of on propagation of hot electrons through plasmas and solid materials

Propagation of hot electrons in plasmas is very important for the fast ignition concept. However, it is impossible to directly investigate the behavior of the in-going hot electrons in plasmas. The propagation characteristics can be only achieved from hot electrons penetrating through plasmas and measured behind the target. Experiments to study this subject were conducted and the results are discussed as follows. We used two kinds of targets. One is 1  $\mu\text{m}$  aluminum film deposited on flat fused glass substrates by laser-plasma deposit technique. The other is simply a 5  $\mu\text{m}$  aluminum film stick parallel on fused glass substrates, with a gap of 20  $\mu\text{m}$  between each other.  $P$ -polarized laser pulses are incident on the target at  $10^\circ$ . Hot electrons produced can pass through the plasma and target remains, then penetrate into the fused glass and ionize it, leaving in the substrate a plasma channel (path), which was monitored by the time resolved shadowgraphy technique. To realize this, a well synchronized laser pulse of 30 fs of 400 nm acts as the probe beam perpendicularly to the plasma channel.

Figure 10a shows a typical shadowgram for the 1  $\mu\text{m}$  Al coated fused glass slide at different time delays after the interaction. In order to enhance the contrast of this particular image, we have subtracted the image of the unperturbed glass substrate in the presence of the probe beam. The dark region in the image corresponds to a plasma density greater than the critical density of 400-nm light,  $6.9 \times 10^{21}/\text{cm}^3$ . Besides the plasmas before the Al film, there is a nearly isotropic dark region behind the Al film. According to the calculated velocity of its expansion edge into the glass ( $2 \times 10^8$  cm/s), this dark region may be attributed to radiation driven thermal transport ionization waves. What interested us is the narrow dark jet within the ionization wave, originating from the interaction region and ending far into the glass.

The self-focused laser light, the hard x-rays and hot electrons can all induce the plasma tracks in the glass. However, the 1  $\mu\text{m}$  Al coating on the glass can block the incident laser during the interacting period. The contrast ratio of the laser pulse is  $10^{-5}$  at 1 ps as measured by a third-order auto-correlator. Numerical simulation suggests that the laser pedestal does not ablate the 1  $\mu\text{m}$  Al film. The shock wave was found to propagate through the 1  $\mu\text{m}$  Al 100 ps later, which is long after the interaction and the hot electron's arrival at

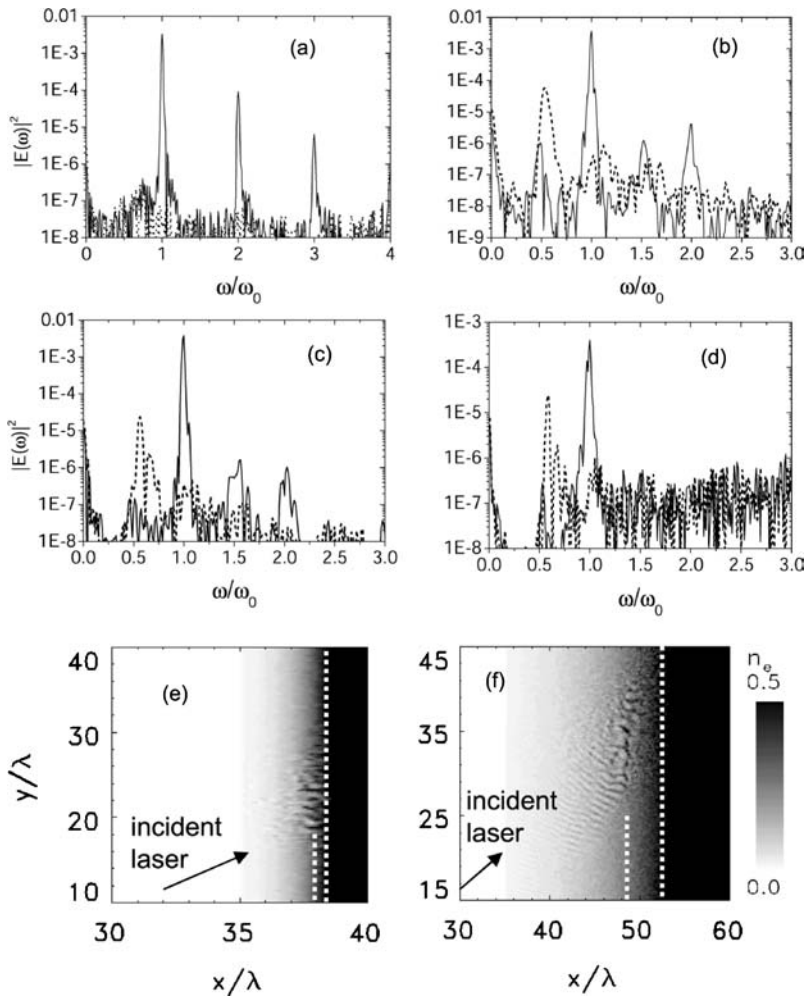


**FIGURE 9** Frequency spectra of reflected light *solid lines* and backscattered light *dotted lines* found from 2D PIC simulations for p-polarized incidence of laser pulses at  $a_0 = 0.2$  and incident angle of  $45^\circ$ . **a**  $L = 0$ ; **b**  $L = \lambda_0$ ; **c**  $L = 3\lambda_0$ ; **d**  $L = 6\lambda_0$ . Frame **e** and **f** show the electron density perturbations at  $L = \lambda_0$  and  $6\lambda_0$ , respectively; The white *dashed lines* mark the layer of the quarter critical density and that of half critical density where the laser pulse is reflected

its journey end in the substrate. Then the presence of laser light filaments in the glass can be ruled out. Strong x-rays are another cause of ionized tracks. A composite target consisting of a  $5\ \mu\text{m}$  Al foil stick on the fused glass is used to investigate this possibility. The basic idea is using the space-charge field in the rear plasma interface with the vacuum to reduce the energy of hot electrons. The space-charge field is estimated to be  $7.6 \times 10^{11}\ \text{V/m}$ , which induces the ionization of the material at the rear surface of the foil, forming the mushroom like plasma as shown by Fig. 10b. Plasma tracks formed in the glass with such composite targets is much shorter than that with the deposited Al film target, excluding the possibility of x-rays ionized plasma channel whose situation is not susceptible to the change of space-charge field.

It is interest to note that in Fig. 10a there are two jets at the center of the focal spot, and several jets parallel but away from the axis of the laser beam. This phenomenon is due to two possible reasons. The first originates from the process of hot electron production. The focal spot is measured to have a full width at half maximum of  $10\text{--}20\ \mu\text{m}$ . When energy is increased, the laser beam quality is strongly modulated by thermal effects and inhomogeneity of the dope concentration in the Ti:sapphire crystal. Thus there exist hot spots in the laser beam. When the beam is focused, the hot spots will become many small local high intensity spots around the focus, which

is sufficiently high to produce hot electrons to induce ionization plasma channels in the fused silica. The second cause is from Weibel instability taking place in the propagation of hot electrons in plasmas. Filaments can happen when the hot electron beam splits. Some filaments are diffused outward from the center of the focal spot, and produce the plasma channel away from the axis of the laser.

## 5 Hot electron generation by relativistic intensity laser pulses

In this section, we will discuss the high energy electrons produced in sub-picosecond laser-plasma interactions from sub-relativistic laser intensities to relativistic intensities when a large scale preplasma presents [57]. The relativistic intensity laser pulses is capable of practical use in the fast ignition, for forward hot electrons along the laser axis can be produced and injected into the compressed core as ignition trigger [1]. Experiments were carried out in ILE, Osaka University. A  $0.61\ \text{ps}$ ,  $1.053\text{-}\mu\text{m}$  linearly polarized laser pulse with an energy up to  $10\ \text{J}$  was focused onto a  $5\ \mu\text{m}$  thick aluminum foil target. The pulse pedestal is about  $3 \times 10^{-3}$  starting from  $700\ \text{ps}$  before the main laser peak [58]. Therefore, the main laser beam interacted with a preplasma generated by the Amplified Spontaneous Emission (ASE) pedestal.

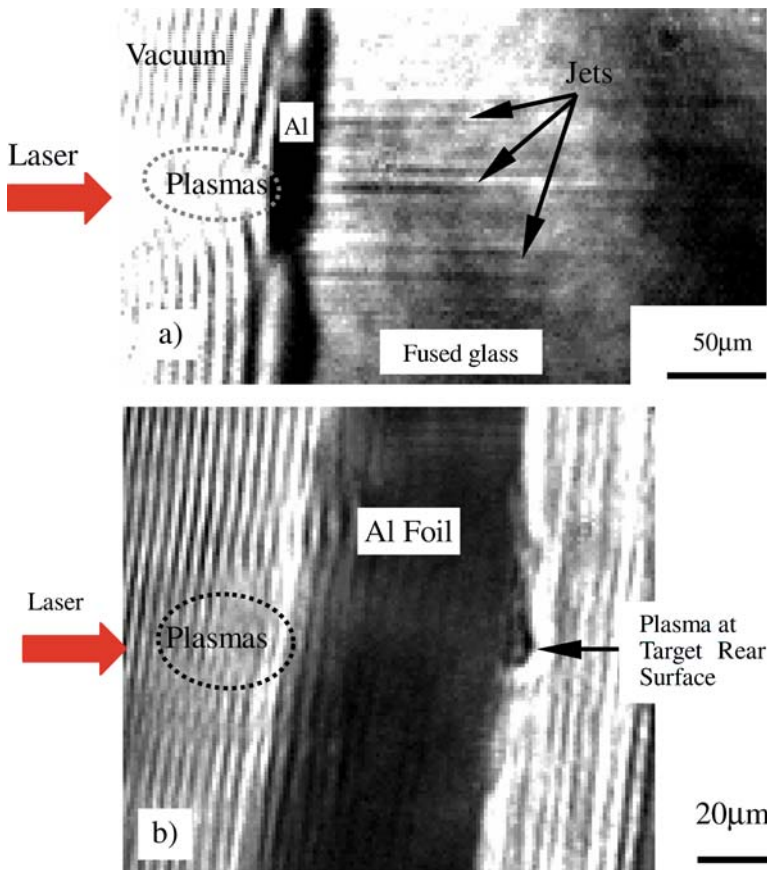


**FIGURE 10** A typical shadowgraph of the plasma channels ionized by hot electrons from the Al film **a** and the mushroom like plasma at the rear of the target **b**

Figure 11a shows the angular distribution of the forward hot electrons behind a 5- $\mu\text{m}$  thick aluminum target illuminated by *p*-polarized laser pulse with an incidence angle of  $45^\circ$  from the sub-relativistic laser intensities to the relativistic. Figure 11b shows the angular distributions of the hot electrons in the laser polarization plane for *s*-polarized laser beam. For *p*-polarization, at  $a_0 \sim 1$ , the widths of the cone angle is larger than those at other intensities. This is reasonable based on the basic understanding of hot electron generation. For  $a_0 < 1$  the main electron acceleration mechanisms are the resonance absorption or vacuum heating etc. Hot electrons are emitted along the density gradient or the normal direction of solid targets. While for  $a_0 > 1$  the hot electrons are accelerated mainly in the longitudinal direction by  $\mathbf{V} \times \mathbf{B}$  force, etc. However, for  $a_0 \sim 1$  these mechanisms compete with each other, so that

a wider cone angle of hot electrons occurs. The location of the spectrum peak falling between the target normal and the laser axis when  $a_0 \leq 1$  indicates the combination effects from the  $\mathbf{V} \times \mathbf{B}$  force and the collective behavior of plasma wave along target normal. Only when the laser intensity is several times larger the laser intensity of  $1.37 \times 10^{18} \text{ W/cm}^2$ , can the hot electron beam turn to the laser propagation direction and become well-collimated.

For *s*-polarization, however, the electron beam is directed to the laser axis, with a maximum fluctuation of  $10^\circ$ . In our previous *s*-polarized femtosecond laser-solid target experiments, for  $a_0$  far less than 1 ( $a_0 \sim 0.1$ ) it has been found that the two well-collimated hot electron beams are emitted in front of the target in the laser polarization direction due to the direct laser field acceleration. When  $a_0$  is between

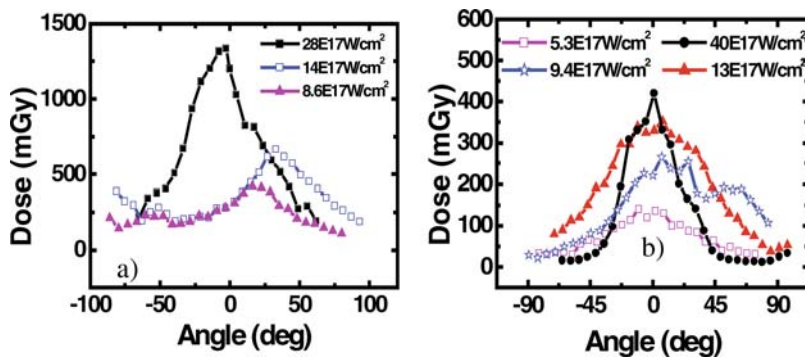


**FIGURE 11** Angular distribution of the forward hot electrons produced by *p*-polarized laser pulse **a** and by *s*-polarized laser pulse at different laser intensities **b**. The curve for the laser intensity of  $40 \times 10^{17} \text{ W/cm}^2$  is reduced by five times in order to compare the data clearly in **b**

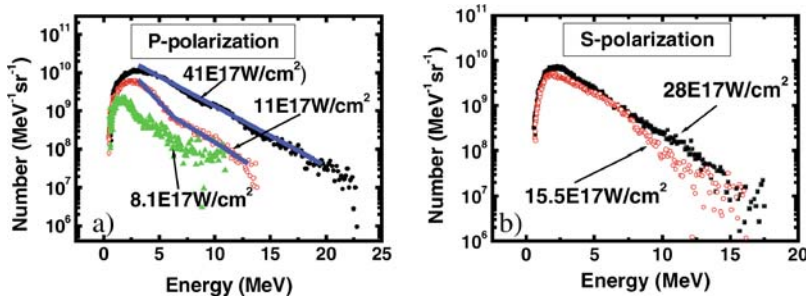


**FIGURE 12** Energy distributions of the forward hot electrons exiting from the aluminum foil for  $p$ -polarized laser pulse **a**,  $s$ -polarized laser pulse **b** at different laser intensities. The solid lines are the exponential fit to the experimental data

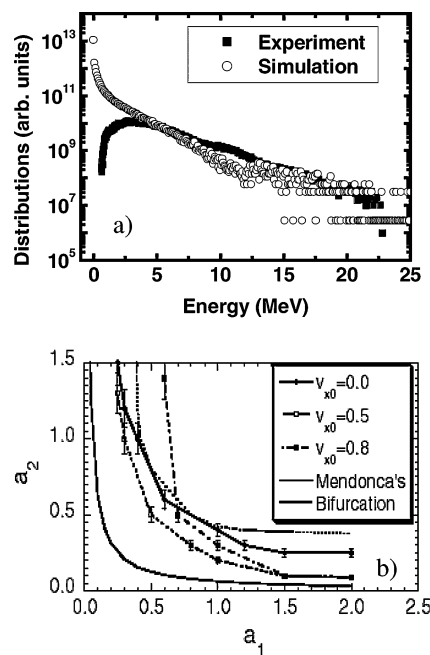
0.1  $\sim$  0.5, the divergence angles of the hot electron beams in front of the target become wider and wider, and the peak positions move to the backward laser vector [43]. In this experiment we find the angular distribution of hot electrons forward through the target shows similar trends. For  $a_0 \leq 1$ , the divergence angles increase with the laser intensity. However, when the laser intensity is several times larger the laser intensity of  $1.37 \times 10^{18}$  W/cm<sup>2</sup> the hot electron beam becomes well-collimated again. This indicates that the forward electron acceleration mechanisms dominate.

Figure 12a and b show the energy spectra of the hot electrons measured behind the foil target for  $p$ -polarized laser pulses and  $s$ -polarized laser pulses at different intensities, respectively. The solid straight lines are the fitting curves using a Boltzmann distribution. We can see that for laser intensities  $a_0 \leq 1$ , two group hot electrons with different effective temperatures can be identified. However, as the laser intensity becomes relativistic ( $a_0 > 1$ ), only one effective temperature presents for both the  $p$ - and the  $s$ -polarization. It is obvious that the longitudinal acceleration mechanism gradually becomes dominant over other mechanisms as the laser intensity is increased to the relativistic. The measured energy of the hot electrons is significant large than that observed in previous experiments [44, 59, 60]. For example, for the  $p$ -polarized laser pulse at an intensity of  $41 \times 10^{17}$  W/cm<sup>2</sup>, the effective temperature obtained by fitting an  $\exp(-E/kT)$  to the tail of the energy distribution is about 3.0 MeV and the maximum energy is up to 20 MeV. Such energy and temperature are much higher than that expected by the ponderomotive potential scaling law [61], and by the empirical scaling law proposed by Beg [62] if  $41 \times 10^{17}$  W/cm<sup>2</sup> is supposed to be the *interacting* intensity when hot electrons are generated. However, such intensity in the present dense plasma is capable of relativistically focusing or even channel trapping the interacting laser pulse, which in turn generates more energetic electrons. Such process was suggested in experiments about the correlation between hot electron features and plasma density scale lengths [63].

To justify this hypothesis experimentally, we used interferometry technique to measure the electron density distribution of the preplasma. No signs of plasma channels were found. Based on the target thickness and the electron density profile measured, we use a 1D3V fully relativistic particle-in-cell (PIC) code to simulate the interactions. The computation conditions are from the experimental parameters. Both the electron spectrum obtained from the PIC simulation and the experimental spectrum for  $p$ -polarized laser pulse are plotted in Fig. 13a. The simulated electron spectrum well reproduces the measured one for the hot electrons with higher energy

(>2MeV). The electrons can be accelerated to energy over 20 MeV. The low-energy hot electrons measured with the spectrometer are seriously affected by the charge separation field at the rear target surface. The number of the low energy hot electrons from the target will be reduced by the reflection and the re-circulation movement of those electrons at the rear target surface [64–66]. However, the PIC simulation spectrum corresponds to the hot electron distribution inside the plasma. This can explain the discrepancy of the simulation and the measurement for the low energy component.

Besides the well-known  $V \times B$  heating mechanism, other hot electron generation mechanisms may also contribute. In the experiments, the backward stimulated Brillouin scattering (SBS) and the stimulated Raman scattering (SRS) can occur in the large scale preplasma the laser ASE produced [67–68]. Our simulation shows that the integrated reflectivity of laser beam is as high as  $\sim 20\%$  at an intensity of several  $10^{18}$  W/cm<sup>2</sup>. The reflected light beams counter-propagates with the incident laser beam. This interaction configuration of two



**FIGURE 13** **a** Comparison of the simulated electron spectrum and the experimental spectrum for  $p$ -polarized laser light at an intensity of  $40 \times 10^{17}$  W/cm<sup>2</sup>; **b** Threshold amplitudes for stochastic motion in the incident ( $a_1$ ) and reflected ( $a_2$ ) laser fields obtained numerically for electrons with different initial velocities. Also shown are the thresholds for local stochastic motion given by Mendonca and for the occurrence of bifurcation for trajectories trapped in the fundamental island around  $(p_x, \eta) = (0, 0)$

colliding laser pulses may accelerate electrons stochastically, producing hot electrons more energetic than  $V \times B$  force [29]. This mechanism works when the laser fields exceed some threshold amplitudes (see Fig. 13b) for stochastic motion of electrons.

Now, we would like to recall the interesting achievements by Kodama et al. [58]. With similar experiment conditions, they demonstrated electron jets in the specular reflection direction. The self-focusing and the possible channel trapping of the reflected laser pulse were invoked as well as the self-generated 20–30 MG quasi-static magnetic field to explain the well collimated electron beam.

The long scale pre-plasmas play essential roles in the several hundred fs relativistically intense laser pulse experiments. To eliminate the uncertainties in determination of the electron acceleration mechanism, experiments were carried out with short intense laser pulses of tens fs FWHM duration. As introduced in Sect. 2, the laser system delivers pulses with contrast ratio better than  $10^{-5}$  at 1 ps pedestal. This helps avoid the long scale pre-plasmas and allow the main body of the incident pulse to interact with the surface of a solid density plasma. The interacting laser pulse is  $s$ -polarized and incident on an Al foil target at  $45^\circ$  from target surface. The measured vacuum intensity of the 31 fs pulse is  $2.1 \times 10^{18} \text{ W/cm}^2$ , smaller than that used above. Shadowgraphy technique measured plasma profile shows only tenuous plasmas before the critical surface. Angular distribution of hot electrons emitted backward were measured. High energy electrons were found to be ejected near the specular reflection, but departed toward the target normal direction. PIC simulations of two spatial dimensions with same parameters were used to explain this observation. We studied the relation between the hot electron emission angle and its energy. Abundant hot electrons were simulated to leave the target forward in the laser propagation direction, the same as observed in Fig. 12 when the intensity was increased to  $41 \times 10^{17} \text{ W/cm}^2$ , but with lower energies. This electron beam is directly accelerated by the ponderomotive force. Another broad electron beam was also generated near the specular reflection, in good agreements with hot electron emission features achieved in the experiments. The second electron beam is attributed to the ponderomotive force acceleration by the reflected laser pulse, as the simulation diagnosis of the laser reflection ratio is determined to be 54%. Both beams are proved to be affected by the space-charge field  $\Phi$  in front of targets. The hot electron emission angle is analytically related to its energy and  $\Phi$  by

$$\tan(\theta) = \left[ \frac{2(\gamma - 1)(1 + \delta\Phi) - \delta\Phi^2}{(\gamma - 1 - \delta\Phi)^2} \sin^{-2}(\alpha) + \tan^{-2}(\alpha) \right]^{-1/2},$$

where  $\alpha$  is the incident angle and equal to  $45^\circ$  in this case.  $\delta\Phi$  is the space-charge field experienced by hot electrons.  $\theta$  and  $\gamma$  is the emission angle and energy of the hot electron, respectively [29]. This formula was used to fit the simulation results. The space-charge field functions by limiting the hot electron ejection angles. Theoretical works suggest that the space-charge fields around the target also play significant roles in the stochastic acceleration process by acting as a ‘disturbing force’ [29]. This can be seen clearly by simulations using an

ultra-thin foil target, which is transparent for the relativistic laser pulses. The laser absorption and the electron acceleration were found enhanced significantly [64]. The effects of the space-charge field both in front and rear of the target is obvious after being fitted with the above formula as shown there.

In summary, the characteristics of hot electrons produced by sub-picosecond laser plasma interactions have been systematically studied for different laser polarizations at relativistic laser intensities. The peak of the hot electron beam produced by  $p$ -polarized laser beam moves expectedly to the laser propagation direction from the target normal direction as the laser intensity is increased to be relativistic. For  $s$ -polarized laser pulse, the hot electrons are directed to the laser axis direction mainly. The maximum energy of the hot electrons is accelerated to as high as 20 MeV and the average temperature of the hot electrons reaches up to 3.0 MeV at a laser intensity  $41 \times 10^{17} \text{ W/cm}^2$ , which is much higher than that expected by the empirical scale law. The energy spectra of the hot electrons evolve to be a single-temperature structure at relativistic laser intensities from the two-temperature structure at sub-relativistic intensities. The existence of a preplasma formed by the laser ASE pedestal plays important role in the interaction. 1D PIC simulations reproduce most characteristics of the experimental measurement. Experiments with 31 fs intense laser pulses have shown the space-charge field effects on the ejection angle of hot electrons.

## 6 Hot electrons from non-relativistic ultrashort laser interactions with liquid droplets

The interaction between ultrashort high-power laser pulses and clusters or micro-liquid droplets attracts significant attentions because of its unique characteristics as the droplets are at a near-solid density but with sub-micron sizes that are comparable to the wavelength of interacting light. Enhancements of laser absorptions and x-ray and hot electron emission are found, and attributed to the successfully weakened electric conductivity in gas cluster where micro-plasmas are located as islands. The resulted hot droplets show prospects of being new sources of x-rays, protons, and even neutrons [69–72]. The absorption of laser energy and the emission of white light, soft x-rays, and hard x-rays in the laser-droplet interactions have been studied. However, only a few publications are involved in the study of hot electron generation from the droplets. In this section we report on measurements of the angular distribution and energy spectrum of hot electrons from ethanol droplets irradiated by linearly polarized 150-fs laser pulses at intensity around  $10^{16} \text{ W/cm}^2$  [73, 74].

Two methods have been used to produce the wavelength-scale droplets in the experiments. One is using a multiple laser pulse train with a separation of 10 ns. The droplets can be produced by the first pulse through condensation of water vapor in the ablation plume and direct explosive emission from the focus, like the generation of nanometer-size and micrometer-size particles by pulsed laser ablation on solid in air [75]. Then the succeeding pulses interact with them. The size of the droplets is within 1–6  $\mu\text{m}$ . The average size is about 3  $\mu\text{m}$ . The other method is using a pulsed valve system. The system consists of a gas line backed with high-pressure

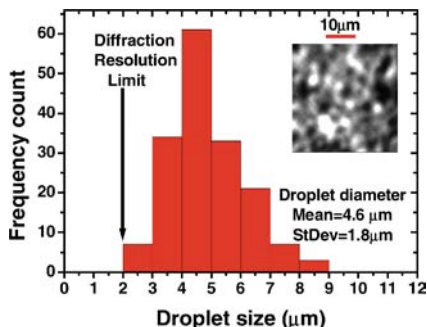


FIGURE 14 Histogram of droplet diameter distribution from ethanol droplets spray ( $T = 300$  K, backing pressure 2 atm.) imaged using the frequency-doubled light of the main laser pulses. The inset shows a typical image of the droplet stream produced by 500  $\mu\text{m}$  orifice

nitrogen, a liquid reservoir with ethanol or water in it, and a solenoid-driven pulsed valve with an orifice. The high-pressure gas along the line propelled the ethanol over the liquid reservoir to stream through the orifice. Thus high density, polydisperse sprays containing several-micron-size liquid droplets can be formed in vacuum. The droplet sizes were measured using an optical imaging system. The droplet spray from the 0.5 mm orifice was back illuminated with frequency-doubled light (395 nm, 150 fs) of the main laser pulses and their shadows were magnified and focused onto a CCD camera. A histogram of size distribution of droplets, shown in Fig. 14, was compiled over many shots. The inset shows a typical magnification image of the droplet spray. The distribution has a mean droplet diameter of 4.6  $\mu\text{m}$ . The number density of the spray is about  $7.9 \times 10^8/\text{cm}^3$ .

Figure 15 displays the spatial distribution of electrons with energies higher than 25 keV produced by multiple pulses at the normal incidence. The dose is accumulated over 10,000 shots. A striking aspect is the presence of two distinct peaks, symmetric with respect to the laser incident direction, in the plane formed by the electric vector and the propagation vector. The direction of the two peaks is at  $46^\circ$  backward from the electric vector with an FWHM (Gaussian profile) of  $34^\circ$ . When the plane of the laser polarization is rotated by  $90^\circ$  using a  $\lambda/2$  wave plate, the direction of the electron emission is found to rotate by  $90^\circ$  correspondingly.

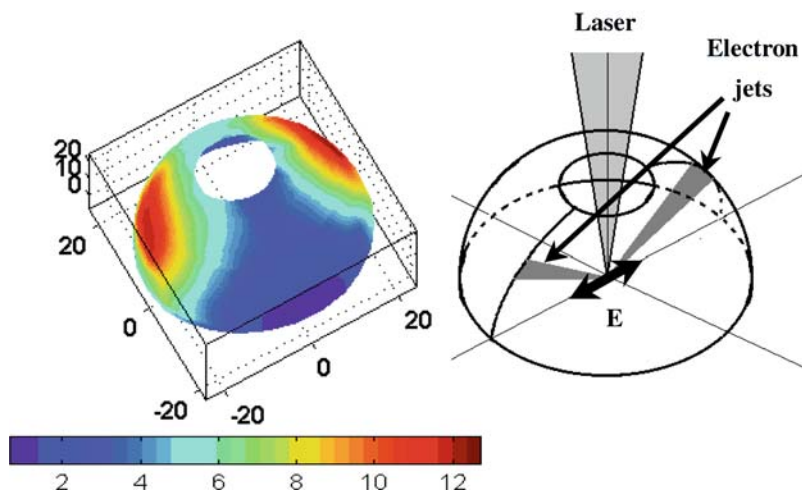


FIGURE 15 Spatial distribution of hot electrons with energies  $> 25\text{keV}$ , produced in the femtosecond laser-droplet interaction

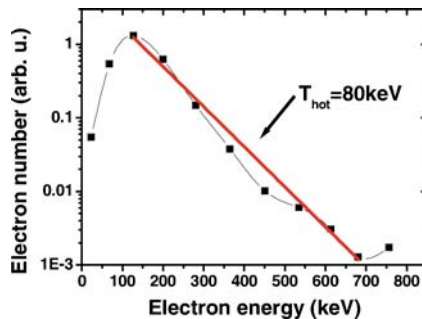
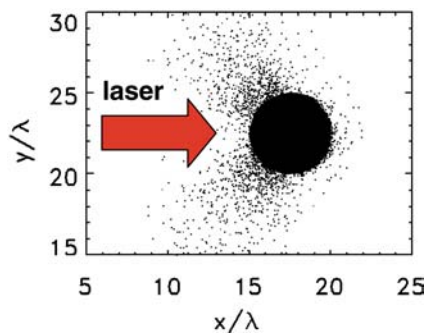


FIGURE 16 A typical hot electron spectrum emitted from the ethanol droplet plasma

Figure 16 shows the energy spectrum of hot electrons from ethanol droplets. The following features are found: 1) the maximum energy of hot electrons is over 600 keV, 2) the number of hot electrons with energies over 300 keV is very low as compared with those with energies less than 300 keV, and 3) the peak of the electron spectrum is around 120 keV. This implies that a charge separation potential was developed and many hot electrons had been pushed back to the droplet surface. Fitting the data to the Maxwellian distribution, an effective temperature of hot electrons, 56 keV, is obtained. This temperature is comparable to the one (66 keV) obtained in laser-solid interactions under similar conditions [76]. It is also comparable to the one (70 keV) found in laser-cluster interactions under the condition that the atomic cluster be irradiated by a laser pulse at a higher intensity ( $10^{17} \text{W}/\text{cm}^2$ ) but with a shorter duration (28 fs) [77].

To explain our experimental results, 2D PIC simulations are performed, where the spherical droplets are approximated as infinitely long cylinders. In the simulations we take  $a_0 = 0.1$ , which corresponds to a laser intensity at focus slightly larger than  $10^{16} \text{W}/\text{cm}^2$  used in our experiment. The laser pulse is incident along the  $x$ -direction from left normally on to the droplet plasma with a diameter of  $5\lambda$ . Initially the electron density increases exponentially along the radial direction of the droplet from  $0.2n_c$  at the droplet edge ( $r = 2.5\lambda$  from the droplet center) until  $2.0n_c$  at  $r = 0.5\lambda$  where  $n_c$  is the critical density. The electron density remains at  $2.0n_c$  from  $r = 0.5\lambda$  until to the droplet center. The corresponding density scale



**FIGURE 17** Snapshots of the electron positions in  $(x, y)$  plot obtained from the 2D PIC simulation resulting at the 50 laser cycles for a plasma droplet irradiated by a linearly polarized laser pulse with its polarization along the  $y$  direction

length below the critical density is  $L = 0.9\lambda$ . We find that both the longitudinal and transverse components of the excited electric field near the critical surface increase with time. When  $t = 50$  laser cycles, these electric fields reach the maximum, which are much stronger than the incident laser electric field. It is exactly the enhanced oscillating electric field around the critical density surface that accelerates the electrons to high energies. Figure 17 shows the electron position in the  $(x - y)$  plot at  $t = 50$ . At 50 laser cycles, it is very apparent that two group electrons are accelerated to high energies symmetrically with respect to the laser axis. The strong emissions range from  $\pm 40^\circ$  to about  $\pm 90^\circ$ . This agrees well with the angular distribution measured in our experiments.

In conclusion, we have directly measured the angular distribution and energy spectrum of hot electrons from droplets irradiated by linearly polarized laser pulses with a duration of 150 fs at the intensity of  $10^{16}$  W/cm<sup>2</sup>. We observed a symmetric structure of the angular distribution of hot electrons and two symmetric peaks of emission directions in large angles from droplets with respect to the laser axis. The temperature of hot electrons emitted from several-micron-size droplets is found to be comparative to that from solid and cluster targets under similar laser parameters. Both the measurements and the 2D PIC simulations suggest that resonance absorption mainly contributes to hot electron generation in laser-droplet interactions.

## 7 Summary

To summarize this topical review, we would like to reiterate the encouraging demonstration of the fast ignition scheme where the increased efficiency by about 50% obtained as compared to the conventional fashion [78]. Experiments were carried out in Osaka, Japan. The large laser facility with several kJ energy was used to achieve the highly compressed fuel core, while an 60 J, 100TW lasers delivers the igniting pulses. However, the inertial confinement fusion project is still at early stage and far from application. Such project is one of the most expensive in the world. But with university-level laser systems employing CPA technique, experiments about physics in the project are possible, which bolsters the study of ICS by making it much more popular. Topics in this review mostly concentrate on the production of hot electrons when CPA laser pulses interact with dense plasma

targets. Application research of the laser-plasma is probably a promising choice among so many during the long-term period project. Monoenergetic electron bunch, ultra-short hard x-ray pulses and many other characteristics of the laser-plasma are under investigations, or may be on the way of applications.

**ACKNOWLEDGEMENTS** This work was supported by the NNSFC (Grant No. 10374115, 60321003, 10425416 and 10390161), the National High-Tech ICF program, the NKBRFSF (Grant No. G1999075200), National Key Laboratory of High Temperature and High Density Plasma and the JSPS-CAS Core University Program on Plasma Physics and Nuclear Fusion.

## REFERENCES

- 1 D. Strickland, G. Mourou, *Opt. Commu.* **56**, 219 (1985)
- 2 M. Tabak, J. Hammer, M.E. Glinsky, W.L. Krueer, S.C. Wilks, J. Woodworth, E.M. Campbell, M.D. Perry, R.J. Mason, *Phys. Plasmas* **1**, 1626 (1994)
- 3 T. Tajima, J.M. Dawson, *Phys. Rev. Lett.* **43**, 267 (1979)
- 4 J.M. Dawson, *Phys. Rev.* **113**, 383 (1959)
- 5 W.B. Mori, *IEEE Trans. Plasma Sci.* **PS-15**, 88 (1987); and references therein
- 6 D.J. Sullivan, B.B. Godfrey, *Proc. AIP Conf. Laser Acceleration Particles* **91**, 43 (1982)
- 7 S.V. Bulanov, V.I. Kirsanov, A.S. Sakharov, *JETP Lett.* **50**, 198 (1989)
- 8 P. Sprangle, E. Esarey, J. Krall, G. Joyce, *Phys. Rev. Lett.* **69**, 2200 (1992)
- 9 H. Hamster, A. Sullivan, S. Gordon, W. White, R.W. Falcone, *Phys. Rev. Lett.* **71**, 2725 (1993)
- 10 A. Modena, Z. Najmudin, A.E. Danger, C.E. Clayton, K.A. Marsh, C. Joshi, V. Malka, C.B. Darrow, C. Danson, D. Neely, F.N. Walsh, *Nature* **377**, 606 (1995); and references therein
- 11 A. Ting, E. Esarey, P. Sprangle, *Phys. Fluids B2*, 1390 (1990)
- 12 E. Esarey, M. Pilloff, *Phys. Plasmas* **2**, 1432 (1995)
- 13 C.G.R. Geddes, Cs. Toth, J. van Tilborg, E. Esarey, C.B. Schroeder, D. Bruhwiler, C. Nieter, J. Cary, W.P. Leemans, *Nature* **431**, 538 (2004)
- 14 S.P.D. Mangles, C.D. Murphy, Z. Najmudin, A.G.R. Thomas, J.L. Collier, A.E. Dangor, E.J. Divall, P.S. Foster, J.G. Gallacher, C.J. Hooker, D.A. Jaroszynski, A.J. Langley, W.B. Mori, P.A. Norreys, F.S. Tsung, R. Viskup, B.R. Walton, K. Krushelnick, *Nature* **431**, 535 (2004)
- 15 G. Malka, J. Fuchs, F. Amiranoff, S.D. Baton, R. Gaillard, J.L. Miquel, H. Pepin, C. Rousseaux, G. Bonnaud, M. Busquet, L. Lours, *Phys. Rev. Lett.* **79**, 2053 (1997)
- 16 A. Pukhov, Z.-M. Sheng, J. Meyer-ter-Vehn, *Phys. Plasmas* **6**, 2847 (1999)
- 17 C. Gahn, G.D. Tsakiris, A. Pukhov, J. Meyer-ter-Vehn, G. Pretzler, P. Thirolf, D. Habs, K.J. Witte, *Phys. Rev. Lett.* **83**, 4772 (1999)
- 18 L.M. Chen, J.J. Park, K.-H. Hong, J.L. Kim, J. Zhang, C.H. Nam, *Phys. Rev. E* **66**, 025402(R) (2002)
- 19 Wei Yu, V. Bychenkov, Y. Sentoku, M.Y. Yu, Z.M. Sheng, K. Mima, *Phys. Rev. Lett.* **85**, 570 (2000)
- 20 M.Y. Yu, W. Yu, Z.Y. Chen, J. Zhang, Y. Yin, L.H. Cao, P.X. Lu, Z.Z. Xu, *Phys. Plasmas* **10**, 2468 (2003)
- 21 D.W. Forslund, J.M. Kindel, E.L. Lindman, *Phys. Rev. Lett.* **30**, 739 (1973); C.S. Liu, M.N. Rosenbluth, R.B. White, *Phys. Rev. Lett.* **31**, 697 (1973)
- 22 Z.-M. Sheng, K. Mima, Y. Sentoku, K. Nishihara, *Phys. Rev. E* **61**, 4362 (2000); W.B. Mori, C.D. Decker, D.E. Hinkel, T. Katsouleas, *Phys. Rev. Lett.* **72**, 1482 (1994)
- 23 G.Z. Sheng, E. Ott, Y.C. Lee, P. Guzdar, *Phys. Fluids* **30**, 526 (1987); A. Borisov, A.V. Borovskiy, O.B. Shiryayev, V.V. Korobkin, A.M. Prokhorov, J.C. Solem, T.S. Luk, K. Boyer, C.K. Rhodes, *Phys. Rev. A* **45**, 5830 (1992)
- 24 Z.M. Sheng, J. Meyer-ter-Vehn, *Phys. Rev. E* **54**, 1833 (1996); Q.L. Dong, Z.-M. Sheng, J. Zhang, *Phys. Rev. E* **66**, 027402 (2002)
- 25 E.A. Jackson, *Phys. Rev.* **153**, 235 (1966); C.S. Liu, M.N. Rosenbluth, *Phys. Fluids* **19**, 976 (1976)
- 26 Y. Cang, Q.L. Dong, H.C. Wu, Z.M. Sheng, W. Yu, J. Zhang, *Chin. Phys. Lett.* **21**, 2414 (2004)
- 27 D.W. Forslund, J.M. Kindel, K. Lee, *Phys. Rev. Lett.* **39**, 284 (1977)

- 28 T.E. Cowan, A.W. Hunt, T.W. Phillips, S.C. Wilks, M.D. Perry, C. Brown, W. Fountain, S. Hatchett, J. Johnson, M.H. Key, T. Parnell, D.M. Pennington, R.A. Snavely, Y. Takahashi, *Phys. Rev. Lett.* **84**, 903 (2000)
- 29 Z.-M. Sheng, K. Mima, Y. Sentoku, M.S. Jovanovic, T. Taguchi, J. Zhang, J. Meyer-ter-Vehn, *Phys. Rev. Lett.* **88**, 055004 (2002); Z.-M. Sheng, K. Mima, J. Zhang, J. Meyer-ter-Vehn, *Phys. Rev. E* **69**, 016407 (2004); J. Meyer-ter-Vehna, Z.M. Sheng *Phys. Plasmas* **6**, 641 (1999)
- 30 M.J. Everett, A. Lai, D. Gordon, K. Wharton, C.E. Clayton, W.B. Mori, C. Joshi, *Phys. Rev. Lett.* **74**, 1355 (1995)
- 31 Z. Wei, J. Zhang, J. Xia, *Science in China* **43**, 1083 (2000)
- 32 J.P. Chambaret, C.L. Blanc, G. Chériaux, P. Curley, G. Darpentigny, P. Rousseau, G. Hamoniaux, A. Antonetti, F. Salin, *Opt. Lett.* **21**, 1921 (1996)
- 33 K. Yamakawa, M. Aoyama, S. Matsuoka, H. Takuma, D. Fittinghoff, C.P.J. Barty, *IEEE J. Select. Topic. Quant. Elect.* **4**, 385 (1998)
- 34 E.B. Treacy, *IEEE J. Quant. Elect.* **5**, 454 (1969)
- 35 G.F. Knoll, *Radiation Detector and Measurement*, 2nd ed. (Wiley, New York, 1989)
- 36 L.M. Chen, W. Yu, J. Zhang, Z.Y. Chen, W.M. Jiang, *Sci. China* **43**, 1202 (2000)
- 37 P. Bilski, M. Budzanowski, P. Olko, P. Christensen, *Radiat. Prot. Dosim.* **66**, 101 (1996)
- 38 J. Zhang, Z.L. Chen, H. Teng, L.M. Chen, Y.T. Li, L.Z. Zhao, Z.Y. Wei, Invited talk on CLEO/Pacific Rim 2001, July 15-19, 2001, Chiba, Japan
- 39 L.M. Chen, J. Zhang, Y.T. Li, H. Teng, T.J. Liang, Z.M. Sheng, Q.L. Dong, L.Z. Zhao, Z.Y. Wei, X.W. Tang, *Phys. Rev. Lett.* **87**, 225001(2001)
- 40 Y. Sentoku, H. Ruhl, K. Mima, R. Kodama, K.A. Tanaka, Y. Kishimoto, *Phys. Plasmas* **6**, 2855 (1999)
- 41 C.I. Moore, A. Ting, S.J. McNaught, J. Qiu, H.R. Burris, P. Sprangle, *Phys. Rev. Lett.* **82**, 1688 (1999)
- 42 D. Pesme, W. Rozmus, V.T. Tikhonchuk, A. Maximov, I. Ourdev, C.H. Still, *Phys. Rev. Lett.* **84**, 278 (2000)
- 43 J. Zhang, J. Zhang, Z.M. Sheng, Y.T. Li, Y. Qiu, Z. Jin, H. Teng, *Phys. Rev. E* **69**, 046408 (2004)
- 44 G. Malka, E. Lefebvre, J.L. Miquel, *Phys. Rev. Lett.* **78**, 3314 (1997)
- 45 W.L. Kruer, *The Physics of Laser Plasma Interaction* (Addison-Wesley, New York, 1988)
- 46 H.M. Milchberg, R.R. Freeman, S.C. Davey, R.M. More, *Phys. Rev. Lett.* **61**, 2364 (1988); J.C. Kieffer, P. Audebert, M. Chaker, J.P. Matte, H. Pépin, T.W. Johnston, P. Maine, D. Meyerhofer, J. Deletrez, D. Strickland, P. Bado, G. Mourou, *ibid.* **62**, 760 (1989); M.M. Murnane, H.C. Kapteyn, R.W. Falcone, *ibid.* **62**, 155 (1989); R. Fedosejevs, R. Ottmann, R. Sigel, G. Kuhnle, S. Szatmari, F.P. Schafer, *ibid.* **64**, 1250 (1990)
- 47 D.F. Price, R.M. More, R.S. Walling, G. Guethlein, R.L. Shepherd, R.E. Stewart, W.E. White, *Phys. Rev. Lett.* **75**, 252 (1995); U. Teubner, J. Bergmann, B. van Wonterghem, F.P. Schafer, R. Sauerbrey, *ibid.* **70**, 794 (1993); A. Ng, P. Celliers, A. Forsman, R.M. More, Y.T. Lee, F. Perrot, M.W.C. Dharma, G.A. Rinker, *ibid.* **72**, 3351 (1994)
- 48 Q.L. Dong, J. Zhang, H. Teng, *Phys. Rev. E* **64**, 26411 (2001)
- 49 M. Zepf, G.D. Tsakiris, G. Pretzler, I. Watts, D.M. Chambers, P.A. Norreys, U. Andiel, A.E. Danger, K. Eidmann, C. Gahn, A. Machacek, J.S. Wark, K. Witte, *Phys. Rev. E* **58**, R5253 (1998)
- 50 S. Bastiani, A. Rousse, J.P. Geindre, P. Audebert, C. Quoix, G. Hamoniaux, A. Antonetti, J.-C. Gauthier, *Phys. Rev. E* **56**, 7179 (1997)
- 51 Th. Schlegel, S. Bastiani, L. Gremillet, J.-P. Geindre, P. Audebert, J.-C. Gauthier, E. Lefebvre, G. Bonnaud, J. Deletres, *Phys. Rev. E* **60**, 2209 (1999)
- 52 P. Zhang, J.T. He, D.B. Chen, Z.H. Li, Y. Zhang, J.G. Bian, L. Wang, Z.L. Li, B.H. Feng, X.L. Zhang, D.X. Zhang, X.W. Tang, J. Zhang, *Phys. Rev. E* **57**, R3746 (1998); L.M. Chen, J. Zhang, H. Teng, Q.L. Dong, Z.L. Chen, T.J. Liang, L.Z. Zhao, Z.Y. Wei, *ibid.* **63**, 036403 (2001)
- 53 E. Lefebvre, G. Bonnaud, *Phys. Rev. E* **55**, 1011 (1997); W.S. Lawson, P.W. Rambo, D.J. Larson, *Phys. Plasmas* **4**, 788 (1997)
- 54 A. Pukhov, Z.-M. Sheng, J. Meyer-ter-Vehn, *Phys. Plasmas* **6**, 2847 (1999)
- 55 F. Brunei, *Phys. Rev. Lett.* **59**, 52 (1987); W.L. Kruer, K. Estabrook, *Phys. Fluids* **28**, 430 (1985); T.-Y.B. Yang, W.L. Kruer, A.B. Langdon, T.W. Johnston, *Phys. Plasmas* **3**, 2702 (1996)
- 56 B.B. Afeyan, E.A. Williams, *Phys. Plasmas* **4**, 3827 (1997); *ibid.* **4**, 3845 (1997)
- 57 Y.T. Li, J. Zhang, Z.M. Sheng, J. Zheng, Z.L. Chen, R. Kodama, T. Matsuoka, M. Tampo, K.A. Tanaka, T. Tsutsumi, T. Yabuuchi, *Phys. Rev. E* **69**, 036405 (2004)
- 58 R. Kodama, K.A. Tanaka, Y. Sentoku, T. Matsushita, K. Takahashi, H. Fujita, Y. Kitagawa, Y. Kato, T. Yamanaka, K. Mima, *Phys. Rev. Lett.* **84**, 674(2000)
- 59 K.B. Wharton, S.P. Hatchett, S.C. Wilks, M.H. Key, J.D. Moody, V. Yanovsky, A.A. Offenberger, B.A. Hammel, M.D. Perry, C. Joshi, *Phys. Rev. Lett.* **81**, 822 (1998)
- 60 U. Teubner, I. Uschmann, P. Gibbon, D. Altenbernd, E. Forster, T. Feurer, W. Theobald, R. Sauerbrey, G. Hirst, M.H. Key, J. Lister, D. Neely, *Phys. Rev. E* **54**, 4167 (1996)
- 61 S.C. Wilks, W.L. Kruer, M. Tabak, A.B. Langdon, *Phys. Rev. Lett.* **69**, 1383 (1992)
- 62 F.N. Beg, A.R. Bell, A.E. Danger, C.N. Danson, A.P. Fews, M.E. Glinsky, B.A. Hammel, P. Lee, P.A. Norreys, M. Tatarakis, *Phys. Plasmas* **4**, 447 (1997)
- 63 M.I.K. Santala, M. Zepf, I. Watts, F.N. Beg, E. Clark, M. Tatarakis, K. Krushelnick, A.E. Danger, T. McCanny, I. Spencer, R.P. Singhal, K.W.D. Ledingham, S.C. Wilks, A.C. Machacek, J.S. Wark, R. Allott, R.J. Clarke, P.A. Norreys, *Phys. Rev. Lett.* **84**, 1459 (2000)
- 64 Q.L. Dong, Z.-M. Sheng, M.-Y. Yu, J. Zhang, *Phys. Rev. E* **68**, 026408 (2003)
- 65 Y. Sentoku, T.E. Cowan, A. Kemp, H. Ruhl, *Phys. Plasmas* **10**, 2009 (2003)
- 66 A.J. Mackinnon, Y. Sentoku, P.K. Patel, D.W. Price, S. Hatchett, M.H. Key, C. Andersen, R. Snavely, R.R. Freeman, *Phys. Rev. Lett.* **88**, 215006 (2002)
- 67 C. Rousseaux, M. Rabec le Gloahec, S.D. Baton, F. Amiranoff, J. Fuchs, L. Gremillet, J.C. Adam, A. Heron, P. Mora, *Phys. Plasmas* **9**, 4261 (2002)
- 68 C. Rousseaux, G. Malka, J.L. Miquel, F. Amiranoff, S.D. Baton, *Ph. Mounaix*, *Phys. Rev. Lett.* **74**, 4655 (1995)
- 69 E.T. Gumbrell, A.J. Comley, M.H.R. Hutchinson, R.A. Smith, *Phys. Plasmas* **8**, 1329 (2001)
- 70 S.J. Mcnaught, J. Fan, E. Parra, H.M. Milchberg, *Appl. Phys. Lett.* **79**, 4100 (2001)
- 71 C. Favre, V. Boutou, S.C. Hill, W. Zimmer, M. Krenz, H. Lambrecht, J. Yu, R.K. Chang, L. Woeste, J. Wolf, *Phys. Rev. Lett.* **89**, 035002 (2002)
- 72 K. Garloff, M. van den Donker, J. van der Mullen, F. van Goor, R. Brummans J. Jonkers, *Phys. Rev. E* **66**, 036403 (2002)
- 73 Y.T. Li, J. Zhang, Z.M. Sheng, H. Teng, T.J. Liang, X.Y. Peng, X. Lu, Y.J. Li, X.W. Tang, *Phys. Rev. Lett.* **90**, 165002 (2003)
- 74 X.Y. Peng, J. Zhang, Z. Jin, T.J. Liang, Z.M. Sheng, Y.T. Li, Q.Z. Yu, Z. Y-Zheng, Z.H. Wang, Z.L. Chen, J.Y. Zhong, X.W. Tang, J. Yang, C.J. Sun, *Phys. Rev. E* **69**, 026414 (2004)
- 75 C.-B. Juang, H. Cai, M.F. Becker, J.W. Keto, J.R. Brock, *Appl. Phys. Lett.* **65**, 40 (1994); H. Schittenhelm, G. Callies, P. Berger, H. Hugel, *J. Phys. D* **29**, 1564 (1996)
- 76 Y.T. Li, J. Zhang, L.M. Chen, Y.F. Mu, T.J. Liang, Z.Y. Wei, Q.L. Dong, Z.L. Chen, H. Teng, S.T. Chun-Yu, W.M. Jiang, Z.J. Zheng, X.W. Tang, *Phys. Rev. E* **64**, 046407 (2001)
- 77 L.M. Chen, J. Park, K.H. Hong, I.W. Choi, J.L. Kim, J. Zhang, C.H. Nam, *Phys. Plasmas* **9**, 3595 (2002)
- 78 R. Kodama, P.A. Norreys, K. Mima, A.E. Danger, R.G. Evans, H. Fujita, Y. Kitagawa, K. Krushelnick, T. Miyakoshi, N. Miyanaga, T. Norimatsu, S.J. Rose, T. Shozaki, K. Shigemori, A. Sunahara, M. Tampo, K.A. Tanakak, Y. Toyama, T. Yamanaka, M. Zepf, *Nature* **412**, 798 (2002)